High Velocity and Real-Gas Effects on Weak Two-Dimensional Shock-Interaction Patterns

John J. Bertin* and Bruce W. Graumann†
The University of Texas at Austin, Austin, Texas
and
Winston D. Goodrich‡
NASA Johnson Space Center, Houston, Texas

Numerical solutions have been generated to study the two-dimensional flow-field which results when supersonic flow encounters double-wedge configurations whose angles are such that the flow includes only weak shock waves. Two numerical codes were developed: one which used the perfect-gas relations (including the ability to vary gamma to "simulate" real-gas effects) and a second which incorporated a Mollier table to define equilibrium air properties. Theoretical surface-pressure and heat-transfer distributions in the interaction-perturbed region along the second wedge were obtained for velocities from 1167 m/sec to 7610 m/sec. At the highest velocity, the weak shock-interaction pattern existed when the sweep angle of the second wedge was as low as 27°. Although no locally severe heating rates were obtained, the dimensionless heat-transfer at a given position increased significantly with velocity. Thus, wind tunnel data for weak shock interactions should not be extrapolated directly to entry flight conditions but should be used to construct a realistic model for the flowfield, which can be used to generate the required aerothermodynamic environment.

Nomenclature

M = Mach number
P = static pressure
$\dot{q}$ = local heat-transfer rate
$\dot{q}_{t,ref}$ = heat-transfer rate at the stagnation point of a reference sphere
R = radius of the reference sphere
S = wetted distance along the second wedge
T = static temperature
U = streamwise velocity
δ = initial turning angle (see Fig. 1)
Λ = sweep angle (see Fig. 1)
$\underset{\sim}{\Lambda}$ = deflection angle of second wedge, complement of sweep angle (see Fig. 1)

Introduction

To determine the complete convective heat-transfer distribution for shuttle entry-configurations flying at hypersonic speeds, one must fully understand and properly model the viscous: inviscid interactions associated with the complex three-dimensional flowfields. Because of the complexity of the viscous: inviscid interaction phenomena, many investigators have studied the locally perturbed flowfields using models consisting of basic elemental patterns. Based on the models of Edney,[1] three types of shock-interference patterns are possible for the wing leading-edge of the shuttle. For small angles of sweep, a Type-IV interaction occurs; for intermediate angles of sweep, a Type-V interaction occurs; and for a highly swept leading-edge, a Type-VI interaction occurs.

Hains and Keyes[2] have categorized shock-interaction patterns obtained for a variety of space-shuttle configurations in terms of the models by Edney. Bertin, et al.,[3] examined surface-pressure and heat-transfer-rate data for a variety of shuttle-orbiter configurations over an angle-of-attack range from 0° to 60.° It was found that the "type" of shock-interaction pattern was dominated by the effective sweep angle of the leading edge. For the relatively low sweep angles of the straight-wing-orbiters, the interaction between the bow-generated shock-wave and the wing-generated shock-wave exhibited the characteristics of a Type-V shock-interference pattern. For the delta-wing orbiters, the shock:shock interaction exhibited the characteristics of a Type-VI pattern for all angles of attack.

The preceding data were obtained in facilities where real-gas effects would not be expected to significantly affect the shock-interaction phenomena. By comparing data from facilities using helium, air, nitrogen, and tetrafluoromethane as the test gases, Hunt and Creel[4] studied the effect of shock-density ratio on the body-shock:wing-shock interaction phenomena. For straight-winged orbiters, the observed movement of the intersection location was found to be strongly dependent on the shock density, or specific-heat ratio. Hunt and Creel concluded that, because the delta-wing configuration "re-enters at lower angles of attack and is essentially free of imbedded shocks, real-gas shock-density-ratio effects will be less significant" than those for the straight-wing orbiter.

The present paper discusses numerical codes which were developed to calculate the two-dimensional flowfield which results when supersonic flow encounters double-wedge configurations whose angles are such that a Type VI pattern occurs. The flowfield models for the numerical codes include the shock-interaction phenomena observed for three-dimensional flows in Ref. 3. However, the three-dimensional shock-interaction pattern for the wing leading-edge of the entry configuration at angle of attack may be substantially different than the two-dimensional flowfield. The present investigation was undertaken to determine the effect of the gas-property model and of the freestream velocity on the surface-pressure and on the heat-transfer distributions on the second wedge for a Type-VI shock-interaction pattern. Two numerical codes were developed: one which used the perfect gas relations (in-

---

Submitted June 13, 1974; presented as Paper 74-522 at the AIAA 7th Fluid and Plasma Dynamics Conference, Palo Alto, Calif., June 17-19, 1974; revision received October 15, 1974. This work was supported in part by the NASA Johnson Space Center under Contract NAS 9-10976.

Index categories: Jet Wakes, and Viscid-Inviscid Flow Interactions; Supersonic and Hypersonic Flows.

*Associate Professor, Department of Aerospace Engineering and Engineering Mechanics. Member AIAA.

†Research Assistant, Department of Aerospace Engineering and Engineering Mechanics.

‡Aerospace Technologist, Aerothermodynamics Section. Member AIAA.

cluding the ability to vary gamma to "simulate" real-gas effects) and a second which incorporated a Mollier table to define equilibrium air properties. Theoretical solutions were obtained for velocities from 1167 m/sec (3821 fps), i.e., a wid-tunnel condition, to 7610 m/sec (25,000 fps), i.e., an entry condition.

Theoretical Analysis

The complex flowfield, which is established when a high-speed flow encounters a double-wedge configuration, is dominated by a shock-interaction region which imposes a highly non-uniform flowfield adjacent to the wedge boundary layer. The shock-interference patterns which are relevant to the wing leading-edge of the shuttle entry-configurations are Type V and Type VI. The Type-V shock-interference pattern causes a shock wave to impinge on the boundary layer, while the Type-VI shock-interference pattern produces an impinging expansion wave.

The numerical code for the Type-V interaction uses a flowfield model (Fig. 1a) which includes: 1) the undisturbed freestream flow; 2) the flow turned through the angle δ by a single shock wave; 3) the flow turned through the angle Λ_s by two shock waves; 4) the flow which has been processed by three shock waves, such that the flow direction and the pressure in region 4 match the corresponding values in region 5; 5) the flow which has been processed by two shock waves, with the second shock wave being a strong shock (with the pressure and flow direction matching those in region 4); 6) the flow which has passes through a curve shock wave, such that the downstream flow is subsonic and parallel to the second wedge; and 7) the flow turned by a reflected shock wave or by a Mach reflection, depending on the flow condition in region 4 and the shock-wave angle.

The numerical code for the Type VI interaction uses a flowfield model (Fig. 1b) which includes: 1) the undisturbed freestream flow; 2) the flow turned through the angle δ by a single wave; 3) the flow turned through the angle Λ_s by two shock waves; 4) the flow processed by the right-running waves of the expansion fan which are centered at the intersection of the two shock waves; 5) the flow which passes through the left running waves produced by the reflection of the waves of the expansion fan; and 6) the flow turned through the angle Λ_s by a single shock wave. The flow in region 3 has passed through two shock waves, while further downstream in region 6 the flow has passed through a single shock wave and is, therefore, at a lower pressure than that in region 3. Thus, although the flow directions are the same, the gas must undergo an expansion from the wedge juncture to equalize the pressure. The flow accelerates isentropically through the expansion region so that the pressure and the flow direction in region 5E are identical to the values for region 6.

Mechanisms of the Limits of the Shock-Interference Pattern

Characteristics of the shock-interference patterns for a double-wedge configuration depend on the deflection angle of the first wedge, the sweep of the second wedge of the model, the freestream flow condition, and the gas-property model. The minimum sweep angle for which a Type-V pattern is possible is that for which a linear, oblique shock wave divides region 2 from region 3. The Type-VI shock interference characteristics no longer exist when the sweep angle becomes so small that the required outboard flow (i.e., that in region 6) can not be generated by a single, weak shock wave. Over a range of geometry both the Type-V and the Type-VI shock-interference patterns can exist numerically for a given geometry subject to a given flow condition. Using the numerical codes developed for the Type-V and Type-VI patterns, the range of sweep angles for which both shock-interference patterns could exist was determined. The range of sweep angles for this overlapping is represented in Fig. 2 for different velocities and for different first wedge deflection-angles. It can be seen that the extent of the overlap increases as the velocity increases.

Schlieren photographs, which were obtained in the Mach 5, University of Texas Supersonic Wind Tunnel,[5] indicate that a

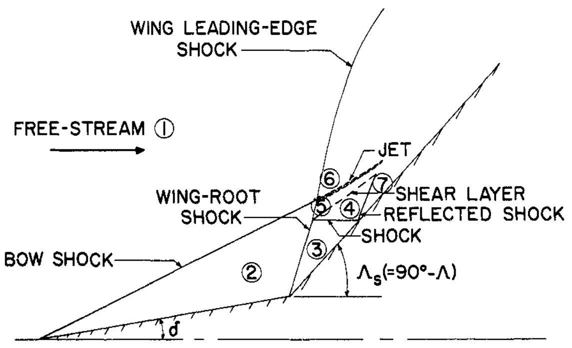

a) TYPE V

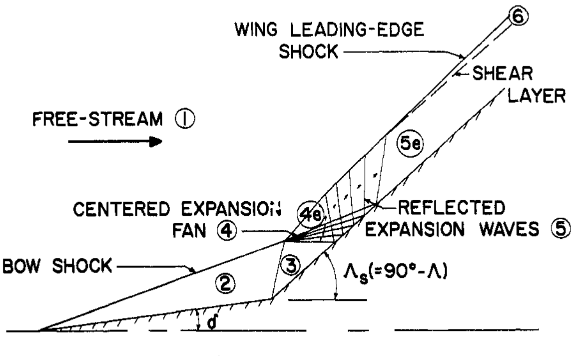

b) TYPE VI

Fig. 1 Flow models of the shock-interaction pattern for a double wedge.

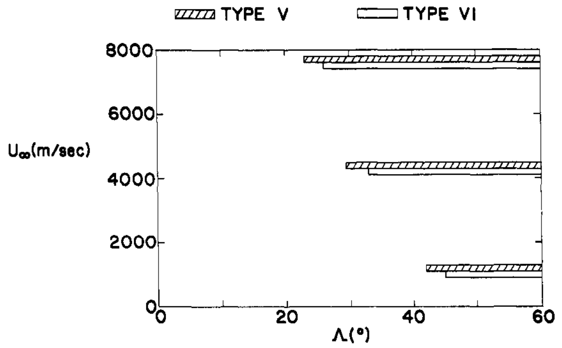

a) δ=5°

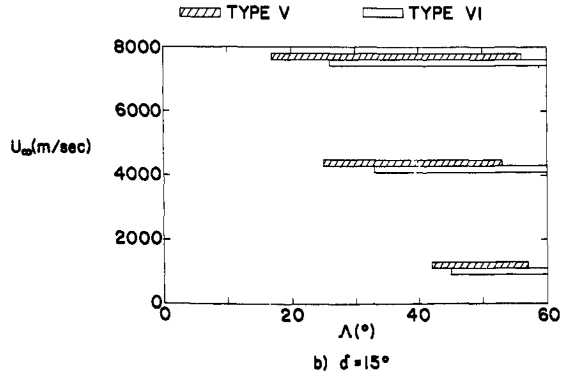

b) δ=15°

Fig. 2 Range of sweep angles for which Type-V and Type-VI patterns are theoretically possible (based on solutions with the real-gas code).

Type-V pattern exists for sweep angles from 40° to 46°, while a Type-VI pattern exists for higher sweep angles. Thus, in the region where either pattern exists theoretically, the weaker solution exists experimentally. These results are consistent with the observation[3] that the shock:shock interaction patterns for the highly swept delta-wing orbiters exhibited the characteristics of a Type-VI pattern as noted previously. Thus, the present study concentrated on the analysis of the Type-VI pattern.

Description of the Numerical Codes for the Type VI Shock-Interaction Pattern

A) Perfect-Gas Code

The first steps were the calculations of the flow conditions downstream of an oblique shock wave for a given flow-deflection angle and for a given gamma, i.e., in regions 2, 3, and 6. The flow conditions in region 5E could then be calculated, since the static pressure in region 5E is equal to the static pressure in region 6 and, under the isentropic-expansion assumption, the stagnation pressure in region 5E is equal to the stagnation pressure in region 3. The expansion process by which the gas accelerates from region 3 to region 5E was divided into ten equal steps. To satisfy the physical boundary condition that the flow in region 5E be parallel to the wall, the total change in the Prandtl-Meyer angle was divided into ten equal parts: the five right-running waves of region 4 and the five reflected waves constituting region 5. Since the current study is concerned with the shock-interaction flowfield phenomena which directly influence the surface (i.e., pressure, shear, and heat transfer), the flowfield properties along the wall were calculated including the interactions between the right-running and the left-running waves in the numerical code. The governing equations for these calculations are summarized in Ref. 6.

Having defined the inviscid flowfield and, hence, the conditions at the edge of the boundary layer, the heat-transfer distribution along the downstream wedge was calculated using the Eckert-reference-temperature technique.[7] For the wind-tunnel flow-condition, where the perfect-gas relations accurately describe the gas behavior, the Eckert-reference-temperature heating rates compared favorably with the values using the nonsimilar boundary-layer code described below. Due to the simplicity of the Eckert method, it was used with the perfect-gas calculations. The boundary layer of the downstream wedge was assumed to originate at the intersection of the two wedges.

One way of approximating the high-temperature, or real-gas, properties of air is to use lower values of gamma in the perfect-gas relations. Therefore, the equations for the perfect-gas code have been written so that one can input one value of gamma for regions 1 and 2, another gamma for regions 3 through 5E, and a third value for region 6. Thus, one can approximate real-gas effects for the varying shock strengths. The perfect-gas code was used to generate three "different" types of solution. For the present paper, these types of solution are referred to as: 1) "perfect-gas" solution for which $\gamma = 1.40$ throughout the flowfield, 2) "constant-gamma" solution for which $\gamma = 1.20$ throughout the flowfield, and 3) "variable-gamma" solution for which different values of gamma were assigned to the three input gamma parameters. (The required values were obtained from the real-gas solutions).

To be consistent in these perfect-gas-code solutions, the specific heat of air was held constant both for the constant-gamma and the variable-gamma solution. Sutherland's relation[6] was used to calculate the viscosity. The Prandtl number was assumed to be 0.7. Thus, the thermal conductivity was uniquely determined.

B) Real-gas code

Philosophically, the calculation procedure for the shock-interaction pattern using the real-gas code was similar to that described for the perfect-gas code. However, to account for the high-temperature, or "real-gas," effects all thermodynamic properties are evaluated using numerical charts for air in chemical equilibrium.[8] Reference 9 was used to define the temperature dependence of the transport properties of equilibrium air, i.e., viscosity, thermal conductivity, and specific heat. Once the shock relations have been used to define the static pressure and the entropy for the two end regions, the expansion from region 3 to region 5E is divided into ten equal steps. The flow conditions in the intermediate regions of the isentropic expansion are calculated using the relations of Ref. 10. The relations require the static enthalpy and the local speed of sound for the intermediate regions, which are evaluated using the tables for equilibrium air.[8]

The heat-transfer distribution along the downstream wedge is calculated using a nonsimilar boundary-layer code,[11] which was modified so that the thermodynamic properties for the viscous flow would also be calculated using Ref. 8. In addition to accounting for the "real-gas" effects, the effect of the acceleration of the inviscid flow is included in the nonsimilar code. As before, the boundary layer is assumed to originate at the junction of the two wedges.

Discussion of Results

Numerical solutions were generated to determine the effect of freestream flow-conditions and gas properties on the flowfield and of the wall temperature on the heat transfer in the region where the Type-VI shock-interaction influenced the second wedge. Flowfield solutions were generated for three freestream conditions: 1) a wind tunnel condition where:

$$U_\infty = 1167 \text{ m/sec}, \; P_\infty = 2.98 \text{ mmHg}, \; T_\infty = 53°\text{K}$$

$$(U_\infty = 3821 \text{ fps}, \; P_\infty = 0.057 \text{ psia}, \; T_\infty = 95°\text{R}$$

2) an orbiter entry condition where:

$$U_\infty = 4330 \text{ m/sec}, \; P_\infty = 0.333 \text{ mmHg}, \; T_\infty = 273\text{K}$$

$$(U_\infty = 14{,}200 \text{ fps}, \; P_\infty = 0.0064 \text{ psia}, \; T_\infty = 491°\text{R}$$

3) an orbiter entry condition where:

$$U_\infty = 7610 \text{ m/sec}, \; P_\infty = 0.0268 \text{ mmHg}, \; T_\infty = 195\text{K}$$

$$(U_\infty = 25{,}000 \text{ fps}, \; P_\infty = 0.00052 \text{ psia}, \; T_\infty = 352°\text{R})$$

Solutions were obtained using both the perfect-gas code and the real-gas code at all flow conditions. The variable-gamma option of the perfect-gas code was used to generate solutions only for flow conditions 2 and 3. Heat-transfer distributions along the downstream wedge were obtained for all three freestream conditions for a wall temperature T_w of 394K (710°R) and for the two entry conditions for a T_w of 1640K (2960°R).

The shock-interference geometry in Fig. 1 was intentionally drawn out of scale so that the various regions could be clearly identified. Presented in Fig. 3 is a typical computed geometry; specifically, a perfect-gas solution for condition 3 with a sweep angle of 60°.

The location and the extent of the interaction-perturbed region are presented in Fig. 4 as a function of the freestream velocity. The limits of the band represent the intersections of the limits of the centered expansion fan, i.e., region 4 of Fig. 1b, with the second wedge. The locations are presented as the distance from the junction of the two wedges (*S*) divided by the radius of a reference sphere (*R*, which is equal to 0.0027m). The "constant-gamma" solution represents those wind tunnels (e.g., Ref. 4) for which the test gas has a relatively low value of gamma, which is to simulate the large density changes associated with hypersonic flight. With the exception of the constant-gamma solution, the various solutions provide similar locations of the interaction-perturbed region over the velocity range considered. At the

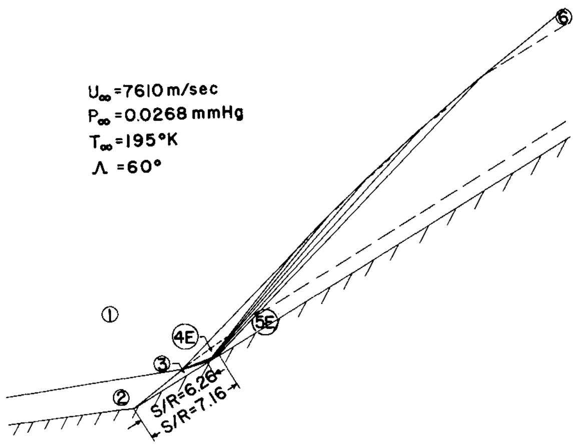

Fig. 3 Calculated geometry of Type-VI shock-interaction pattern for a perfect-gas solution.

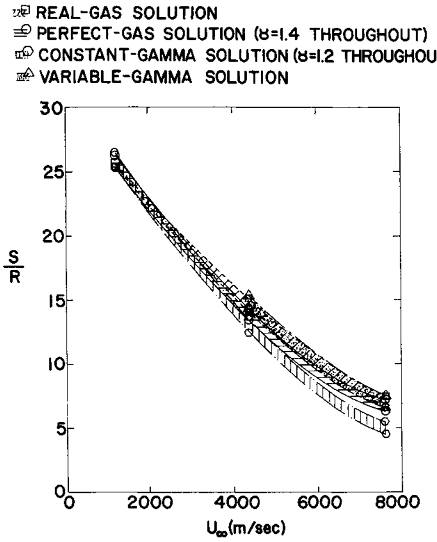

Fig. 4 Location of the interaction-perturbed region on the downstream wedge (which was swept 60°) as a function of velocity and of gas-property assumption.

higher velocities, the interaction-perturbed region is relatively inboard for the constant-gamma solution, because the shock angle for γ= 1.20 is nearer the surface than is the shock angle for γ= 1.40. However, because the actual γ is essentially unchanged for the first deflection angle for the two flight conditions, the real-gas solution and the perfect-gas solution yield essentially identical results for the shock-interaction location. At the low (wind-tunnel) velocity, the constant-gamma solution for the interaction region correlates with the other solutions because both the bow shock angle and the "simulated leading-edge" shock angle are relatively small, producing compensating effects.

Surface-pressure distributions along the second wedge are presented in Fig. 5. For the wind-tunnel condition, i.e., condition 1, the perfect-gas solution (γ = 1.40 everywhere) and the real-gas solution are in essential agreement. The differences between these solutions were attributed to the difficulty of using the Mollier Tables at these low temperatures and were relatively small. Thus, the perfect-gas solution of Fig. 5a also represents the real-gas solution. The constant-gamma solution yields pressures which are significantly lower than the other two solutions. As noted previously, both the angles for the bow shock and for the "leading-edge" shock are relatively small for γ = 1.20 and, therefore, the interaction region for γ = 1.20 nearly coincides with those of the other two solutions.

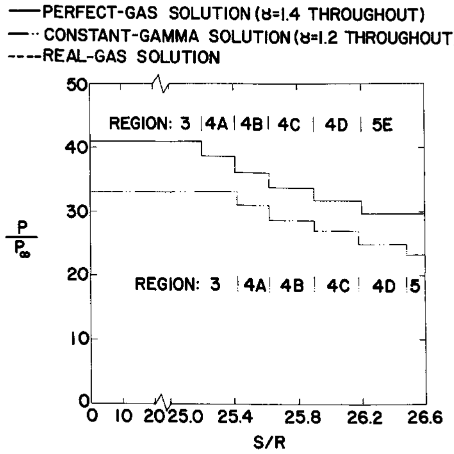

a) CONDITION 1: U_∞=1167m/sec, P_∞=2.98mmHg, T_∞=53°K

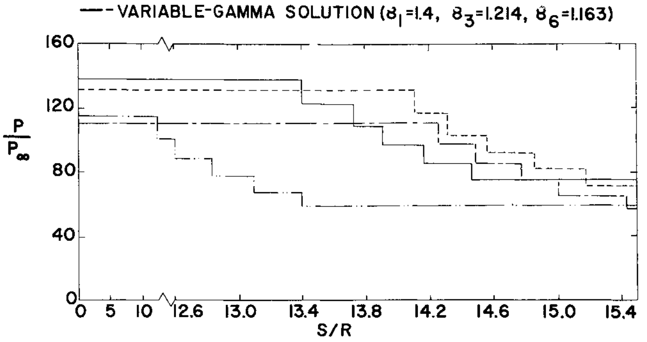

b) CONDITION 2: U_∞=4330m/sec, P_∞=0.333 mmHg, T_∞=273°K

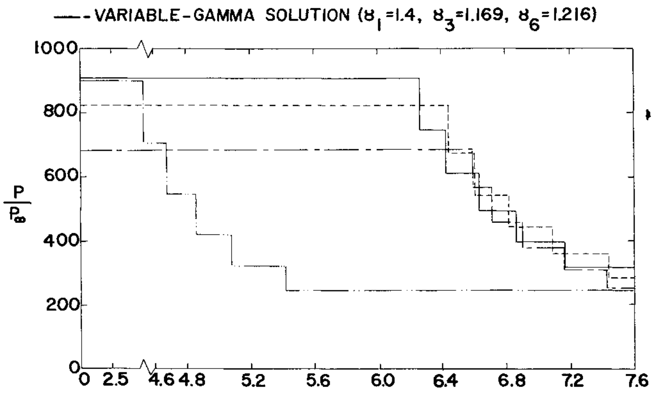

c) CONDITION 3: U_∞=7610m/sec, P_∞=0.0268 mmHg, T_∞=195°K

Fig. 5 Surface-pressure distribution along the second wedge.

For the middle velocity condition (Fig. 5b), the shock-interaction region for the constant-gamma solution is inboard relative to the other solutions. It has been noted that the difference is due to the fact that the initial shock wave is weak and, therefore, does not significantly alter gamma from its actual freestream value of 1.40. When comparing the pressure from a given region, the constant-gamma value is lower than the real-gas value by approximately the same amount that the perfect-gas value is higher than the real-gas output to define the gamma variation, are significantly below the real-gas values. However, as might be expected, the location of the interaction-perturbed region provided by the variable-solution corresponds to the location provided by the real-gas solution.

For condition 3 (Fig. 5c), the constant-gamma pressures in corresponding regions of the expansion fan are in very good agreement with the perfect-gas pressure for that region, both being somewhat higher than the real-gas values. Again,

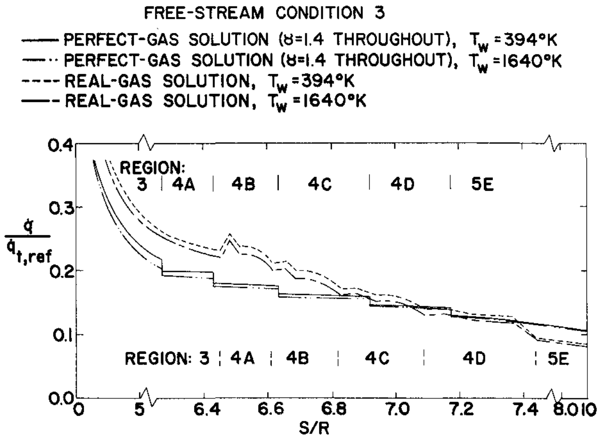

Fig. 6 Effect of surface temperature on heat-transfer distribution along the second wedge.

however, because the bow shock-wave generated by the initial turning of the flow is much closer to the body when $\gamma = 1.20$ than it is for the real-gas solution or for the perfect-gas solution, the constant-gamma interaction region is markedly inboard. Again, the variable-gamma solution locates the interaction-perturbed region but underpredicts the pressure relative to the real-gas solution.

The local heat-transfer rates have been normalized by $\dot{q}_{t,ref}$, the stagnation point heating rate[12] for a reference sphere whose radius was chosen to be 0.0027 m and which is at the same temperature as the wedge surface. The dimensionless heat-transfer parameter $\dot{q}/\dot{q}_{t,ref}$ (or, since the wall temperatures are equal, the approximately equivalent ratio of heat-transfer coefficients) is commonly used in shuttle applications. Heat-transfer distributions were calculated for wall temperatures of 394K and of 1640K. As can be seen in Fig. 6, the wall-temperature variation had no significant effect on the theoretical heat-transfer distributions. The differences between the perfect-gas heat-transfer and the real-gas heating are greatest in regions 3 and 4A, i.e., near the junction of the two wedges and in region 5E, i.e., downstream of the interaction.

The local increases in the real-gas heat-transfer distributions which are evident at the beginning of each flow region are due to the local acceleration of the inviscid flow. In the computer codes, the waves of the expansion fan define a step-function decrease in pressure and a corresponding step-increase in the local velocity at the edge of the boundary layer. Thus, the nonsimilar boundary-layer solutions yield local increases in heating due to the local velocity gradient. There are no locally severe heating rates (which could cause design problems), indicated either in the real-gas solutions or in the perfect-gas solutions. However, the flow model for the present calculations does not include imbedded shock waves or other three-dimensional flow phenomena, which might occur near the actual wing-root fairing. Such flow phenomena caused local increases in heating to delta-wing orbiter configurations.[3]

The heat-transfer distributions for the second wedge with 60° sweep are compared in Fig. 7 for perfect-gas, constant-gamma, variable-gamma, and real-gas solutions. For the wind-tunnel flow condition, i.e., condition 1, the nondimensionalized heat-transfer rates are significantly lower for the perfect-gas solution ($\gamma = 1.40$) than for the constant-gamma solution ($\gamma = 1.20$). Recall that the perfect-gas pressures were significantly higher than the constant-gamma values. Since the gas constant and the Prandtl number were assumed to be constant for the various solutions using the perfect-gas code, the heat-transfer differences reflect the effect of gamma on the local Mach number and on the other parameters of the Eckert-reference-temperature technique. As noted previously, the surface affected by the shock interaction

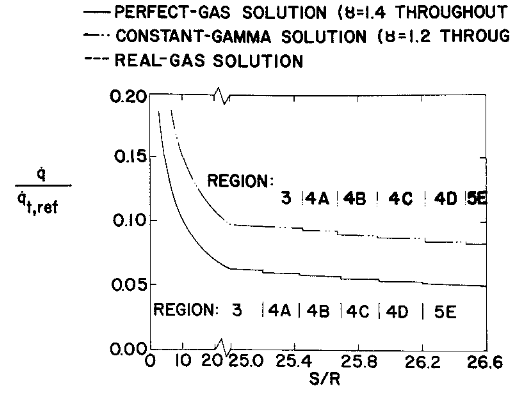

a) CONDITION 1: U_∞=1167 m/sec, P_∞=2.98 mmHg, T_∞=53°K

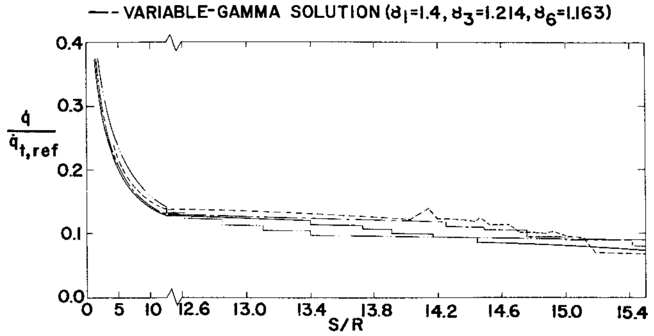

b) CONDITION 2: U_∞=4330m/sec, P_∞=0.333mmHg, T_∞=273°K

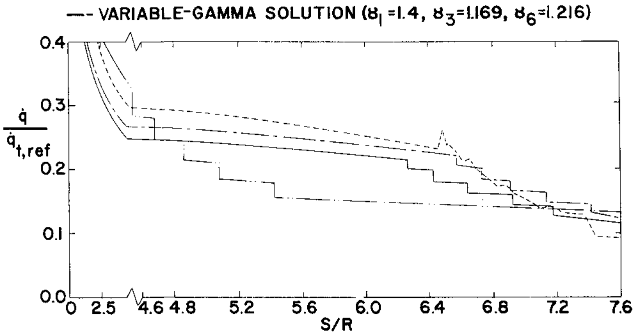

c) CONDITION 3: U_∞=7610m/sec, P_∞=0.0268mmHg, T_∞=195°K

Fig. 7 Heat-transfer-rate distribution along the second wedge.

was approximately the same for the two gas models for this particular flow condition.

The solutions obtained using the real-gas code are compared with solutions obtained using the various options of the perfect-gas code for the two flight conditions in Figs. 7b and 7c. The nondimensionalized values of the heat-transfer rates depend on the gas model used. The differences are most pronounced for the highest velocity condition considered. The differences in the local nondimensionalized heat-transfer-rates near the junction of the two wedges are accentuated by variations in the location of the interaction-perturbed region.

The location and the extent of the interaction perturbed region of the second wedge for the real-gas solutions are presented in Fig. 8 as a function of sweep. The limits of the band represent the intersections of the limits of the centered expansion fan, i.e., region 4 of Fig. 1b, with the second wedge. Calculated locations from the real-gas solutions are presented for sweep angles from 60° down to the minimum sweep angle for which a Type VI pattern exists. The minimum sweep angle decreases as the freestream velocity increases. For the higher velocity entry-condition, the Type-VI pattern is possible for sweep angles as low as 27.° The perturbed region moves inboard toward the wedge junction as the velocity increases.

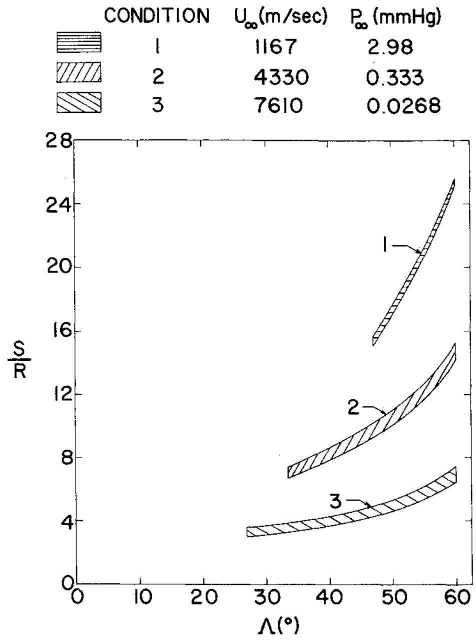

Fig. 8 Location and extent of the interaction-perturbed region for real-gas solutions with $\delta = 5°$ as a function of sweep angle of the second wedge.

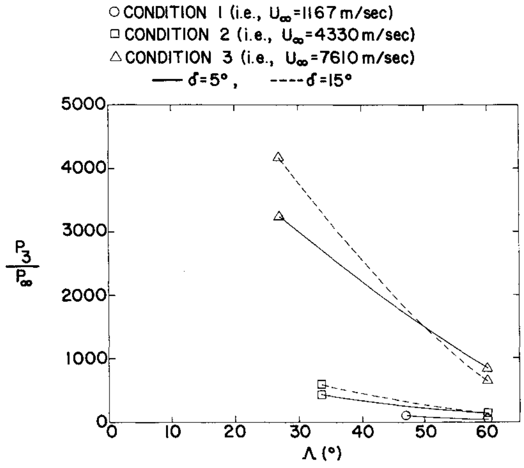

Fig. 9 Pressure inboard of the interaction region as a function of δ and of Λ

The pressure near the junction of the wedges, which is the maximum value, is presented in Fig. 9 as a function of δ and of leading-edge sweep. The flow conditions in region 3 are attained by two linear, oblique shock waves. As would be expected, the pressure increases as the freestream velocity increases and as the sweep angle decreases. Increasing the initial deflection angle from 5° to 15° produces as much as a twenty-five per cent increase in the pressure in region 3.

The pressure ratio across the interaction region is presented in Fig. 10 as a function of δ and of sweep. The pressure ratio across the expansion fan decreases as the velocity increases. An initial deflection of 5° produces only a weak shock wave, and correspondingly a small change in flow conditions. Therefore, for δ of 5,° the ratio $P_6 = P_3$ is essentially independent of sweep angle for the sweep angle range studied. Recall that the pressure in region 6 depends only on the freestream flow condition and the deflection angle of the second wedge. Therefore, the variation of P_6/P_3 with the initial deflection-angle is due to the dependence of P_3 on δ, as indicated in Fig. 9.

The nondimensionalized heat-transfer rate is presented in Fig. 11 as a function of the sweep angle for the second wedge

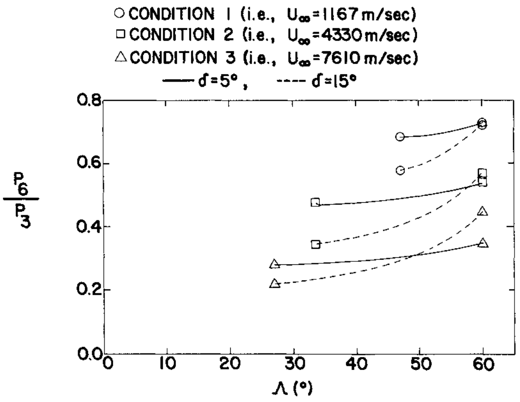

Fig. 10 Pressure variation across the interaction region as a function of δ and of Λ

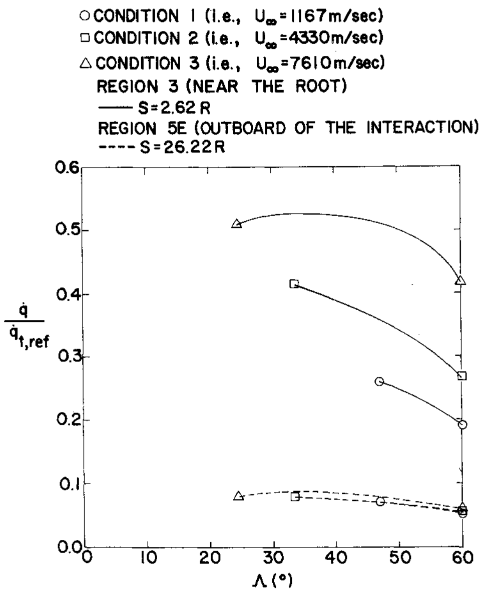

a) δ=5°

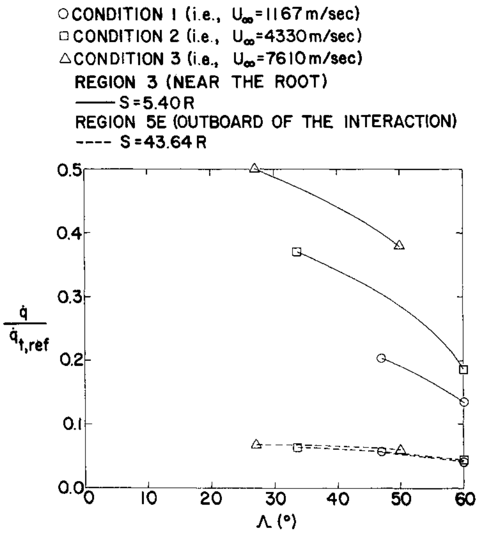

b) δ=15°

Fig. 11 Local heat-transfer rate as a function of sweep angle and the flow condition.

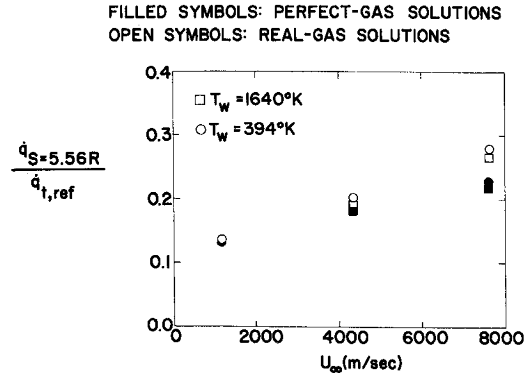

a) POINT IN REGION 3, Λ = 60°

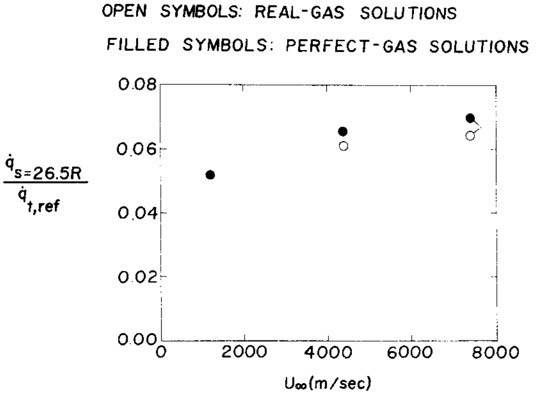

(b) POINT IN REGION 5E, Λ=60° (T = 394° K ONLY)

Fig. 12 Effect of freestream velocity and wall temperature on the heat transfer to the second wedge for δ = 15.°

for a point in region 3, which is inboard of the interaction, and for a point in region 5E, which is outboard of the interaction. Since the interaction-perturbed region moves inboard as the velocity increases, the point in region 3 is near the inboard edge of the interaction region for the highest velocity. Correspondingly, the point of region 5E is near the outboard edge for the lowest velocity. Outboard of the interaction region, the dimensionless heat-transfer rates are essentially independent of the flow condition and of the sweep angle. However, inboard of the interaction region, the nondimensionalized heat transfer increases significantly as the velocity increases and as the sweep angle decreases.

The magnitude of the variation in heat transfer with velocity is a function of location relative to the expansion fan (see Fig. 11). For both the perfect-gas solutions and the real-gas solutions and for both wall temperatures, the nondimensionalized heat-transfer rate increases significantly with velocity inboard of the interaction region (see Fig. 12a). The dimensionless heating for the higher entry velocity is roughly twice that for the wind-tunnel condition for region 3. Outboard of the interaction region, the heat-transfer ratio is much less sensitive to velocity (see Fig. 12b). This implies that one should not extrapolate wind-tunnel data directly to flight conditions. Instead the wind-tunnel data should be used to construct a viable model of the flowfield. The flowfield model can then be used to generate the required aerothermodynamic environment at the conditions of interest.

Conclusions

Based on the calculations of the present study, the following conclusions are made:

1) At the higher entry velocity, the Type-VI interaction pattern existed for "wing leading-edge" sweep angles as low as 27°.

2) For the deflection angles (δ) considered, gamma was not appreciably changed by the weak, first shock wave in the real-gas solution. Thus, perfect-gas (gamma of 1.4) solutions for the flow geometry were in reasonable agreement with the real-gas solutions. The use of the effective gamma did not adequately represent real-gas effects in the surface-pressure distribution.

3) The correlation between the perfect-gas solution and the real-gas solution for the heat-transfer distribution was essentially independent of the wall temperature but depended on the freestream velocity. The heat-transfer distributions for the variable-gamma solution correlated closely with the real-gas heat-transfer distributions.

4) The local, dimensionless heat-transfer rates increased significantly with velocity. The increase occurred both for the perfect-gas solutions and for the real-gas solutions and for both wall temperatures. Thus, one should not extrapolate wind-tunnel data directly to flight conditions. Instead the wind-tunnel data should be used to construct a realistic model for the flowfield, which can be used to generate the required aerothermodynamic environment.

References

[1] Edney, B., "Anomalous Heat Transfer and Pressure Distributions on Blunt Bodies at Hypersonic Speeds in the Presence of an Impinging Shock," Rept. 115, 1968, The Aeronautical Research Institute of Sweden, Stockholm.

[2] Hains, F.D. and Keys, J. W., "Shock Interference Heating in Hypersonic Flows," *AIAA Journal,* Nov. 1972, Vol. 10, pp. 1441-1447.

[3] Bertin, J.J., Graumann, B.W., and Goodrich, W.D. "Aerothermodynamic Aspects of Shock-Interference Patterns for Shuttle Configurations During Entry," *Journal of Spacecraft and Rockets,* Vol. 10, No. 9, Sept. 1973, pp. 545-546.

[4] Hunt, J.L. and Creel, T.R., Jr., "Shock-Interference Heating and Density-Ratio Effects, Part II—Hypersonic Density-Ratio Effects," *NASA Space Shuttle Technology Conference,* Vol. I-Aerothermodynamics, Configurations, and Flight Mechanics, TMX-2272, April 1971, NASA.

[5] Bertin, J.J., Graumann, B.W., and Goodrich, W.D. "Analysis of High-Velocity and Real-Gas Effects on the Shock-Interference Pattern for Delta-Wing Orbiters," AIAA Paper 74-522, Palo Alto, Calif., June 1974.

[6] Ames Research Staff, "Equations, Tables, and Charts for Compressible Flow," Rept. 1135, 1953, NACA.

[7] Eckert, E.R.G., "Engineering Relations for Friction and Heat Transfer to Surfaces in High Velocity Flow," *Journal of the Aeronautical Sciences,* Vol. 22, No. 8, Aug. 1955, pp. 585-587.

[8] Moeckel, W.E. and Weston, K.C., "Composition and Thermodynamic Properties of Air in Chemical Equilibrium," TN 4265, April 1958, NACA.

[9] Hansen, C.F., "Aproximations for the Thermodynamic and Transport Properties of High Temperature Air," TR R-50, 1959, NASA.

[10] Hayes, W.D. and Probstein, R.F., *Hypersonic Flow Theory, Vol. I-Inviscid Flow,* Ch. 7, Academic Press, New York, 1966.

[11] Bertin, J.J. and Byrd, O.E., Jr., "The Analysis of a Nonsimilar Boundary Layer—A Computer Code (NONSIMBL)," Aerospace Engineering Rept. 70002, 1970, The University of Texas at Austin, Austin, Texas.

[12] Fay, J.A. and Riddell, F.R., "Theory of Stagnation Point Heat Transfer in Dissociated Air," *Journal of Aeronautical Sciences,* Vol. 25, Feb. 1959, pp. 73-85, 121.